GSA DATA REPOSITORY 2017293   **Miller et al. (2017)**

Samples Descriptions

Iron oxide environments sampled for this study fall into three groups: (i) lateritic weathering profiles; (ii) ferruginized colluvia; and (iii) channel iron deposits.

Lateritic weathering profiles sit directly on top of iron rich rock, in the case of the Hamerlsey region, on top of a banded iron formation (BIF). A lateritic ferricrust grows downward as seasonal rainfall in combination with plant-derived organic acids triggers the dissolution of BIF minerals, leaving voids for subsequent goethite precipitation (Lascelles, 2012; Kneeshaw and Morris, 2014). This process produces a vitreous goethite cap often meters to tens of meters thick, with small fragments of remnant original hematite present (Kneeshaw and Morris, 2014). Our samples collected from Metawandy Valley represent typical lateritic weathering profile material developed on a BIF (Figure DR1a).

On the flanks of the BIF landforms, ferruginized colluvia encompass another iron-rich environment in the Hamersley region. These deposits are dominated by hematite alluvium with preserved original BIF textures cemented by vitreous goethite (Kneeshaw and Morris, 2014). The Roy Hill samples in this study represent such ferruginized colluvia deposits (Figure DR1d).

Channel iron deposits are ferruginized paleochannels, primarily found in low valleys but also extending onto surrounding plains, dominated by pisoliths, ferruginized wood and goethite cement (Ramanaidou et al., 2003; Kneeshaw and Morris, 2014). The large stream channel size (10s of m wide), long length (sometimes hundreds of km), gentle gradients, meandering form, and wide geographic occurrence indicate these were well-developed river systems during a time Western Australia had a more active

hydraulic cycle than today (Ramanaidou et al., 2003). The Lynn Peak (Figure DR1c) and Yandi (Figure DR1b) samples in this study represent typical CID material.

Natural goethites produced by weathering reactions can range widely in physical and chemical properties, from a disseminated yellowy stain to dense, compact, pure, and highly crystalline masses. Only the latter material was selected for this work. A subset of the samples reported on here were previously characterized by optical microscopy, XRD, SEM, and electron microprobe analysis (Heim et al., 2006; Heim, 2007; Vasconcelos et al., 2013). In this subset, XRD and high-resolution synchrotron analyses yield sharp symmetrical peaks, suggesting a high degree of goethite crystallinity (Heim, 2007; Vasconcelos et al., 2013). Illustrative reflected light photomicrographs and SEM images are shown in Figure DR2. These results are typical of the samples analyzed here.

Goethite may contain variable abundances of SiO_2 (possibly as a discrete phase), as well as substitution of Al for Fe within the mineral structure (Schwertmann, 1988). These impurities might affect either the He age or the oxygen isotope composition of our goethites. Table DR-2 reproduces previously published Al and Si data on a subset of samples analyzed in this study, including specimens from all four studied localities. Si spot analyses range from 0.10 - 2.93 wt % (Heim, 2007; Vasconcelos et al., 2013), with the average Si content of individual samples ranging from 0.29 wt. % to 1.71 wt. % (Table DR2). Al spot analyses range from below detection to 5.90 wt. %, with the average Al content of individual samples ranging from 0.01 wt. % to 4.07 wt. % (Table DR2). We observe no correlations between Al or Si content and He age or oxygen isotope composition within our data set. For example, while the Yandi samples have the most variable Al and Si content, they are not anomalous (nor anomalously variable) in $\delta^{18}O$ or GHe age.

Table DR1: Sample locations and brief descriptions

Sample	Northing	Easting	Host Rock	Depth
Stop1-6-A1	-22.747	116.612	Lateritic ferricrust	Surface
Stop1-6-A7	-22.747	116.612	Lateritic ferricrust	Surface
Stop1-6-A5	-22.747	116.612	Lateritic ferricrust	Surface
Stop1-1-A3	-22.747	116.612	Lateritic ferricrust	Surface
Yan-02-09	-22.721	119.080	CID	Surface
Yan-02-02	-22.721	119.080	CID	Surface
Yan-02-01-A	-22.721	119.080	CID	Surface
Yan-02-03	-22.721	119.080	CID	Surface
Yan-02-06	-22.721	119.080	CID	Surface
Yan-02-01-D1	-22.721	119.080	CID	Surface
LynP-02-09-A5	-22.50	-120.09	CID	Surface
LynP-02-09-A3	-22.50	-120.09	CID	Surface
LynP-02-09-A2	-22.50	-120.09	CID	Surface
LynP-02-09-A1	-22.50	-120.09	CID	Surface
Roy-02-02-Cy1	-22.452	119.930	Ferruginized colluvia	Surface
Roy-02-02-Cy2	-22.452	119.930	Ferruginized colluvia	Surface
Roy-02-02-Cy3	-22.452	119.930	Ferruginized colluvia	Surface
Roy-02-02-B5	-22.452	119.930	Ferruginized colluvia	Surface
Roy-02-02-Co3	-22.452	119.930	Ferruginized colluvia	Surface
Roy 02-02-C1	-22.452	119.930	Ferruginized colluvia	Surface
Roy-02-02-B1	-22.452	119.930	Ferruginized colluvia	Surface

Table DR2: Summary of electron microprobe analyses

Sample	Average Al (wt. %)	n	Min Al (wt. %)	Max Al (wt %)	Average Si (wt. %)	Min Si (wt. %)	Max Si (wt. %)
Stop-1-6-A1*	0.01	9	BD	0.05	1.02	0.87	1.20
Stop-1-6-A5*	0.11	4	0.09	0.14	1.71	1.67	1.79
Stop-1-6-A7*	0.05	5	0.05	0.10	1.38	1.79	1.89
Yan-02-01-A*	1.62	10	0.17	4.94	1.35	0.69	2.93
Yan-02-02*	3.62	6	2.53	4.95	0.76	0.67	0.87
Yan-02-03*	4.07	7	3.40	4.50	1.58	1.32	1.80
Yan-02-06*	0.45	15	0.11	1.45	0.56	0.08	0.88
Yan-02-09*	0.43	10	0.23	0.96	0.97	0.88	1.14
LynP-02-09-A1 [†]	0.64	23	0.11	2.37	0.29	0.15	0.97
LynP-02-09-A2 [†]	2.30	38	0.15	5.90	0.36	0.10	1.65
LynP-02-09-A3 [†]	1.08	20	0.26	3.24	0.42	0.13	2.79
Roy-02-02-B5*	0.03	30	0.00	0.05	0.84	0.68	0.99
Roy-02-02-B1*	0.02	30	0.00	0.03	0.86	0.69	0.95

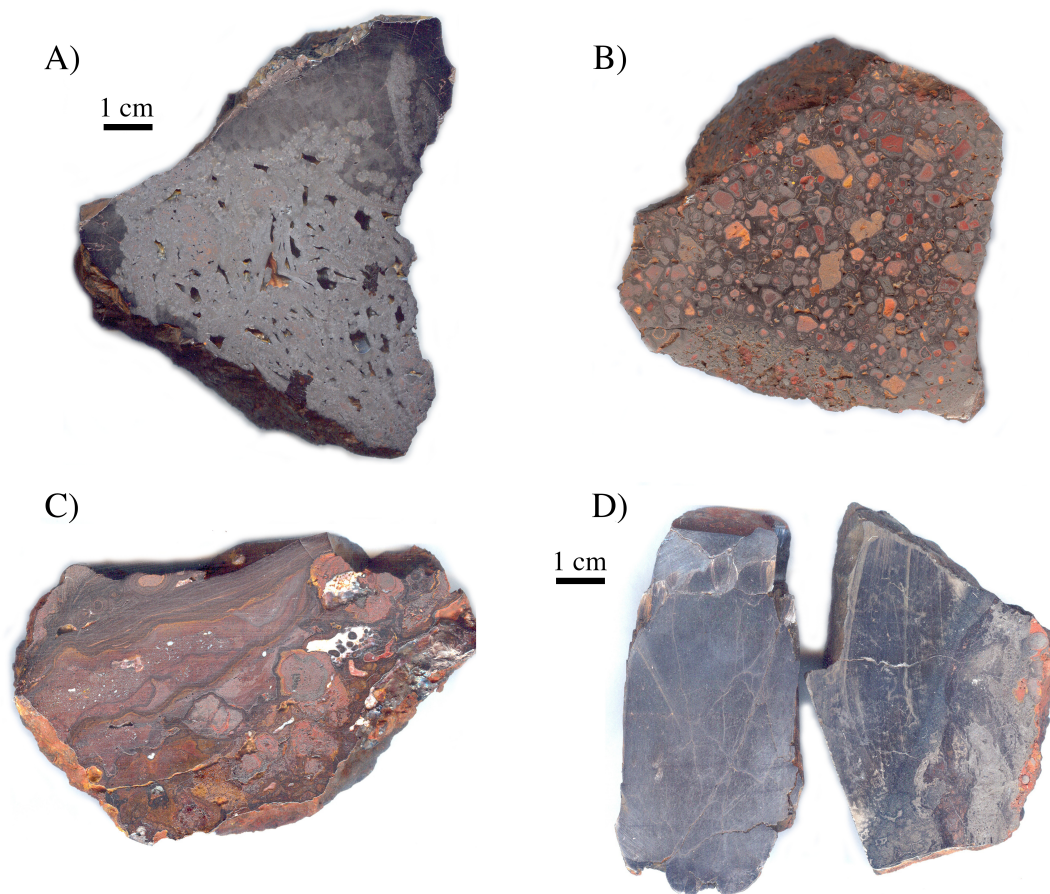* (Heim, 2007); [†] (Vasconcelos, 2013) BD - below detection. n - number of points analyzed.

Figure DR1: Cut hand samples show characteristic textures of each locality from this study. (A) Botryoidal goethite crystals formed in cavities at Metawandy Valley; (B) pisolith and detrital hematite clasts supported in a goethite matrix at Yandi and (C) Lynn Peak; (D) elongate fibrous crystals of Roy Hill.
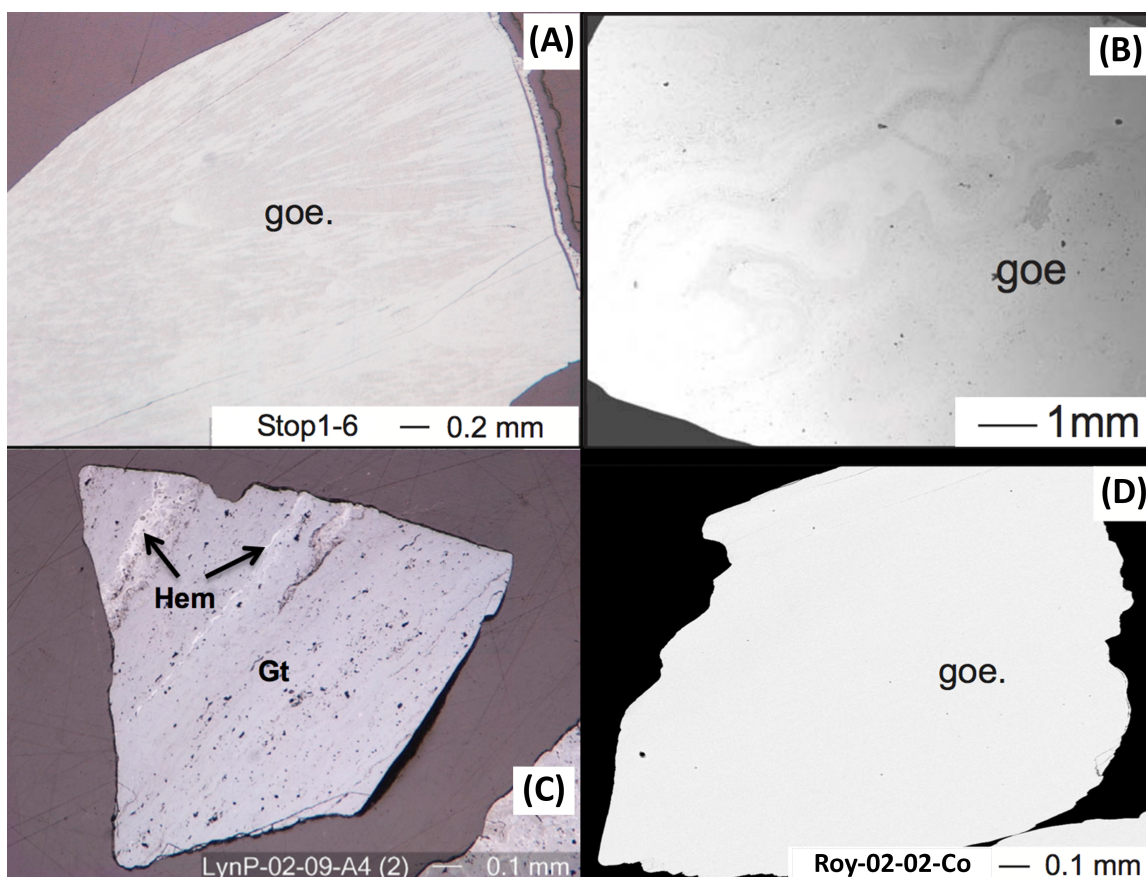
Figure DR2: (A) Representative reflected light photomicrograph of Metawandy Valley sample Stop-1-6, with fibrous crystal growth habit visible. (B) SEM image showing Yandi CID goethite, the darker zones represent greater Al substitution. See Table DR2 for measurements of Al concentration. (C) Reflected light photomicrograph of LynP-02-09-A4, showing the presence of both hematite (Hem) and goethite (Gt). Mixed mineralogy samples such as this one were not analyzed for (U-Th)/He ages or oxygen isotope composition. (D) A SEM image of Roy Hill sample Roy02-02-Co showing our preferred material for geochronology and oxygen isotope analysis: this goethite has uniform composition and low abundance of Al and Si (see Table DR2).

(U-Th)/He chronometry

GHe ages were determined following the procedures of Shuster et al. (2005) and Vasconcelos et al. (2013). Two to three 0.1 to 3 mm fragments (~100 ug) were selected for coarse, crystalline texture, then individually packaged in Pt tubes, heated by laser, and ^{4}He concentrations measured by quadrupole mass spectrometer following cryogenic separation of He and the addition of ^{3}He spike. After complete degassing, the goethite grains within Pt tubes were transferred to a Teflon beaker containing ^{230}Th and ^{235}U spikes and dissolved in concentrated HCl by heating for 12 hours to 90 °C. The spiked solutions were diluted and U and Th concentrations analyzed by quadrupole inductively coupled plasma–mass spectrometry (ICP-MS).

All samples were dated in duplicate or triplicate, and mean GHe ages are reported. The analytical uncertainty of ±2% underestimates the true uncertainty on formation age because most goethites lose at least a few % of their ^{4}He under earth surface conditions (Shuster et al., 2005). For example, ^{4}He/^{3}He experiments on Lynn Peak goethites show that these samples experienced ~5% He loss (Vasconcelos et al., 2013). In the absence of ^{4}He/^{3}He experiments on all of our samples, we make an approximate correction for this effect by assuming 10% He loss and conservatively assign a ±10% uncertainty to all He ages (e.g., as in Monteiro et al., 2014).

Table DR3: New (U-Th)/He results

	Corrected Age (Ma)	±	U (ppm)	Th (ppm)	He (nmol/g)	Mass (µg)
Stop1-6-A1-A	4.5	0.5	5.62	0.16	0.13	72
Stop1-6-A1-B	5.6	0.6	5.15	0.09	0.14	49
Stop1-6-A1-C	4.4	0.4	5.54	0.15	0.12	64
Mean	**4.8**		**5.4**	**0.1**	**0.1**	
Stop1-6-A7-A	4.9	0.5	4.46	0.12	0.11	35
Stop1-6-A7-B	4.9	0.5	4.55	0.03	0.11	41
Mean	**4.9**		**4.5**	**0.1**	**0.1**	
Stop1-6-A5-A	7.5	0.8	5.23	0.11	0.20	19
Stop1-6-A5-B	9.6	1.0	4.94	0.07	0.24	32
Mean	**8.5**		**5.1**	**0.1**	**0.2**	
Stop1-1-A3-A	25.8	2.6	2.86	0.04	0.37	67
Stop1-1-A3-B	26.2	2.6	2.79	0.08	0.37	64
Mean	**26.0**		**2.8**	**0.1**	**0.4**	
Roy-02-02-Cy1-A	44.3	4.4	1.36	1.26	0.36	48
Roy-02-02-Cy1-B	48.3	4.8	1.28	1.27	0.38	53
Roy-02-02-Cy1-C	49.3	4.9	1.15	0.40	0.30	59
Mean	**47.3**		**1.3**	**1.0**	**0.3**	
Roy-02-02-Cy2-A	65.6	6.6	0.69	0.17	0.24	48
Roy-02-02-Cy2-B	60.8	6.1	0.75	0.26	0.25	35
Roy-02-02-Cy2-C	58.6	5.9	0.98	0.32	0.31	78
Mean	**61.7**		**0.8**	**0.3**	**0.3**	
Roy-02-02-Cy3-A	66.9	6.7	1.16	0.32	0.41	73
Roy-02-02-Cy3-B	61.1	6.1	1.55	0.21	0.49	69
Roy-02-02-Cy3-C	76.0	7.6	1.13	0.35	0.46	78
Mean	**68.0**		**1.3**	**0.3**	**0.5**	
Roy-02-02-B5-A	69.3	6.9	1.38	0.09	0.48	64
Roy-02-02-B5-B	66.7	6.7	1.18	0.08	0.40	58
Mean	**68.0**		**1.3**	**0.1**	**0.4**	
Roy-02-02-C1-A	70.5	7.1	1.19	0.04	0.42	63
Roy-02-02-C1-B	71.2	7.1	1.18	0.07	0.42	58
Roy-02-02-C1-C	69.8	7.0	1.22	0.05	0.43	51
Mean	**70.5**		**1.2**	**0.1**	**0.4**	
Roy-02-02-Co3-A	72.3	7.2	1.25	0.09	0.46	60
Roy-02-02-Co3-B	62.9	6.3	1.43	0.17	0.46	44
Roy-02-02-Co3-C	71.2	7.1	1.33	0.11	0.48	94
Mean	**68.8**		**1.3**	**0.1**	**0.5**	

Measurement of stable oxygen isotopes in goethite

Using the sample material recovered from the same initial 4 mm drill core that geochronometry aliquots were selected from, 10 mg of goethite was crushed to 100-300 micron size, sieved, and ultrasonically cleaned in ethanol. A ~2 mg aliquot of sample was heated to 80° C under vacuum overnight and then pretreated with BrF_5 vapor at room temperature to remove any remaining adsorbed water. The sample was then irradiated with a 10.6 μ CO_2 laser while exposed to BrF_5 vapor, driving fluorination reactions that produce O_2, HF and iron fluoride. The O_2 was isolated and purified by cryogenic separation and passage over hot mercury, then converted to CO_2 by passage over hot graphite and analyzed by dual inlet gas source mass spectrometry in that form (Sharp et al., 1990). A garnet standard, UWG-2, was measured throughout each analytical session to monitor the accuracy of each session's measurements. When the measured $\delta^{18}O$ of UWG-2 varied from the known value, a correction was applied, typically ~0.10‰ (Valley et al., 1995). The final pressure of CO_2 produced from a sample fluorination reaction and subsequent CO_2 conversion was measured and used to check that a sample was completely fluorinated, as partial sample fluorination may induce isotopic fractionation (Valley et al., 1995). Analyses were discarded (~25% of total analyses made) when the measured moles of CO_2 differed from the mass-based prediction by more than 10%. In the case of samples with published (U-Th)/He ages, the material prepared for $\delta^{18}O_{goe}$ was sourced from remaining crushate produced from texturally uniform bands within the 4 mm cores used for the original (U-Th)/He analyses.

Table DR4: All Laser Fluorination δ¹⁸O results

Sample	Subsample	$\delta^{18}O_{VSMOW}$ (‰)	±
Stop1-6-A5		-0.370	0.024
Stop1-6-A1		-0.316	0.015
Stop1-6-A7		-0.207	0.033
		-0.228	0.028
		-0.107	0.041
Mean		-0.181	
Stop1-1-A3		-1.257	0.035
		-1.176	0.014
		-0.888	0.027
		-0.873	0.022
Mean		-1.049	
Yan-02-01-A		0.677	0.026
Yan-02-01-D1		0.727	0.055
Yan-02-02		0.703	0.022
Yan-02-03		0.976	0.028
Yan-02-09		0.627	0.027
Yan-02-06		-0.088	0.028
LynP-02-09-A1	A	-0.945	0.016
	A	-0.977	0.022
	B	0.324	0.019
	B	0.188	0.047
	B	-0.069	0.028
	C	-0.872	0.030
	D	-1.002	0.034
Mean		-0.479	
LynP-02-09-A2		-0.714	0.027
		-0.576	0.045
Mean		-0.645	

Table DR4: All Laser Fluorination δ¹⁸O$_{VSMOW}$ results (continued)

Sample	Subsample	δ¹⁸O$_{VSMOW}$ (‰)	±
LynP-02-09-A3	A	0.569	0.037
	A	0.522	0.033
	B	-0.509	0.024
	B	-0.920	0.029
	C	-0.500	0.029
	C	-0.390	0.027
Mean		-0.205	
LynP-02-09-A5		0.613	0.038
		0.543	0.034
Mean		0.578	
Roy-02-02-Cy1		-1.855	0.030
		-1.387	0.048
		-1.231	0.060
		-1.434	0.040
Mean		-1.477	
Roy 02-02-C1		-1.037	0.039
		-1.189	0.040
Mean		-1.113	
Roy-02-02-Co3		-1.629	0.023
		-1.631	0.030
Mean		-1.630	
Roy-02-02-Cy2		-1.533	0.046
		-1.685	0.046
Mean		-1.609	
Roy-02-02-Cy3		-1.654	0.034
		-1.710	0.025
Mean		-1.682	
Roy-02-02-B5		-1.283	0.035
Roy-02-02-B1		-1.928	0.020

Stable oxygen isotope measurements of large-mass samples

We found unexpectedly large $\delta^{18}O$ variability in some of our samples. The reproducibility of UWG-2 standards, the mineralogical purity of goethite in this study (Heim et al., 2006; Heim, 2007; Vasconcelos et al., 2013), and the reproducible $\delta^{18}O$ results from the remainder of our samples together suggest this variability is not inherent to the fluorination procedure or other aspects of the analytical method. As an alternative, we hypothesize that some of our samples contain isotopic heterogeneity arising from factors occurring on short timescales and therefore over small length scales of goethite growth. If so, we expect that replicate measurements of small samples (2 mg) will yield the same mean as analysis of a much larger sample mass. To test this hypothesis, we measured the $\delta^{18}O$ of two of the anomalously variable goethite samples with five times more than our typical sample mass. Weighed samples and standards are typically loaded into a nickel disc with 36 pits. For this experiment, we loaded five adjacent pits each with the ~2 mg sample mass typical of laser fluorination measurements, then drew a proportionally larger quantity of BrF_5 to completely fluorinate the larger mass sample, and lased them all. Typical pretreatment, fluorinated species purification, and CO_2 conversion were all followed for these large-mass measurements. We allowed for a lower yield criterion in these large-mass measurements due to very slow conversion to CO_2. We suspect that the graphite rod reaches a saturation state when exposed to gas from these large mass fluorination reactions and incompletely converted our sample to CO_2.

Larger aliquots produced $\delta^{18}O_{goe}$ results consistent with the average of the smaller aliquots. Thus we interpret these observations to indicate that in some of our samples, 2 mg aliquots were too small to capture the average composition of the goethite. This fine scale heterogeneity may be due to local variations in meteoric

water on time scales unresolvable by GHe dating. By averaging the $\delta^{18}O$ of the smaller aliquots, we obtain our best estimate of the composition of the goethite at the time associated with the GHe age.

Table DR5: Large mass $\delta^{18}O_{VSMOW}$ measurements

Aliquot	Yield (%)	Mass (mg)	$\delta^{18}O_{VSMOW}$ (‰)	±
LynP-02-09-A1 (1A)	82.7	10.72	-0.615	0.018
LynP-02-09-A1 (1B)	89.8	6.96	0.024	0.038
LynP-02-09-A3 (1A)	80.4	11.04	0.270	0.019
LynP-02-09-A3 (1B)	81.3	7.52	0.031	0.015

Table DR6: Comparison between normal mass and large mass measurements

A) LynP-02-09-A1

Normal Mass Aliquots

Number	7
Average $\delta^{18}O$ (‰)	-0.479
Total mass analyzed (mg)	10.78
$\delta^{18}O$ (‰) High Value	0.324
$\delta^{18}O$ (‰) Low Value	-1.002
Range $\delta^{18}O$ (‰)	1.326

Large Mass Aliquots

Number	2
(Mass weighted) Average $\delta^{18}O$ (‰)	-0.363
Total mass analyzed (mg)	17.68
Difference between average of normal mass and large mass $\delta^{18}O$ (‰)	**0.116**

B) LynP-02-09-A3

Normal Mass Aliquots

Number	6
Average $\delta^{18}O$ (‰)	-0.205
Total mass analyzed (mg)	9.02
$\delta^{18}O$ (‰) High Value	0.569
$\delta^{18}O$ (‰) Low Value	-0.920
Range $\delta^{18}O$ (‰)	1.489

Large Mass Aliquots

Number	2
(Mass weighted) Average $\delta^{18}O$ (‰)	0.173
Total mass analyzed (mg)	18.56
Difference between average of normal mass and large mass $\delta^{18}O$ (‰)	**0.378**

(U-Th)/He age to paleolatitude transformations

(U-Th)/He ages were transformed to paleolatitude for each sample to explore the possible correlation between the modern latitudinal gradient in isotopic composition of meteoric water and our $\delta^{18}O_{goe}$ record. Absolute plate speed and direction calculated by Muller et al. (2016) for the Australian plate from 80 Ma to present was used to determine paleolatitudes. The vector along which the center of the Australian plate traveled shifted from NW to NE with a speed of 1-3 cm/yr between 80 Ma and 40 Ma then increased speed significantly to between 6 and 8 cm/yr in the NNE direction between 40 Ma and present (Muller et al., 2016). Table DR7 presents the speed and direction of the Australian plate in 10 Ma periods used to transform (U-Th)/He ages into paleolatitudes. Here we assume the ±10% uncertainty applied to the (U-Th)/He ages dominates over the error associated with determining finite plate rotations and therefore the error assigned to sample paleolatitude is the result of propagating (U-Th)/He error through the latitude transformation. For Cenozoic plate reconstructions, where an absolute reference frame can be tied down via well-constrained subduction and hotspot locations, this assumption is likely valid (Muller et al., 2016).

Table DR7: (U-Th)/He age to paleolatitude conversion rates

Age Range (Ma)	Centimeters per year	Plate direction (azimuth degrees)	Kilometers north per 10 Ma
0 - 10	7.5	15	724.4
10 - 20	7	15	676.1
20 - 30	8	15	772.7
30 - 40	6	20	563.8
40 - 50	3	30	259.8
50 - 60	3	50	192.8
60 - 75	1	-60	50.0

Table DR8: Compiled IAEA meteoric water data from South Pacific

Latitude	Long-term Mean* $\delta^{18}O_{VSMOW}$ (‰)	Standard Deviation	GNIP code
-21.23	-3.77	0.67	9184300
-23.70	-2.90	1.72	9432600
-27.47	-3.49	0.89	9457600
-31.94	-3.11	0.34	9460800
-31.99	-3.74	0.47	9460801
-34.93	-4.01	0.47	9467500
-35.12	-4.50	0.39	9301100
-37.81	-4.63	0.63	9486800
-40.68	-3.59	0.6	9495400
-43.02	-5.04	1.31	9497001
-46.43	-6.89	0.41	9384400

The Global Network of Isotopes in Precipitation (GNIP) is part of the International Atomic Energy Agency's (IAEA) efforts to monitor the distribution and transportation of rare isotopes across our planet. Long-term mean refers to the mean of the annual mean rainwater $\delta^{18}O$ over the lifespan of the collection site, which range between 6 and 54 years.
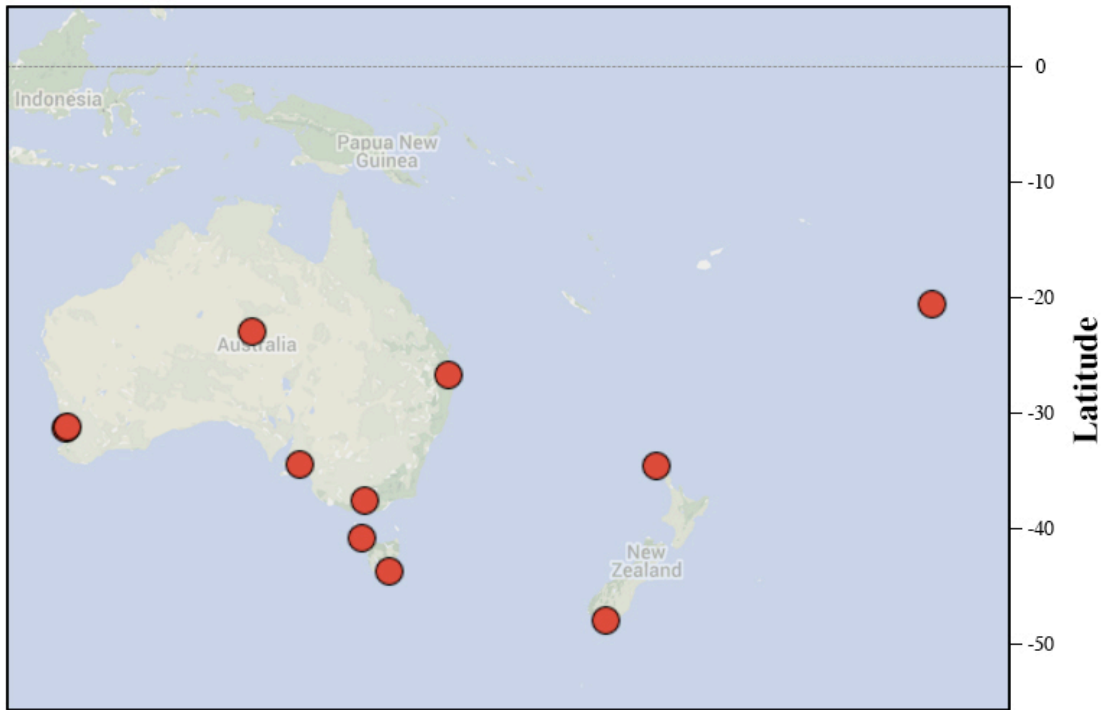

Figure DR3: Red circles show locations of IAEA GNIP collection sites used in this study to create a regional latitudinal gradient in the isotopic composition of rainwater.

References

Heim, Jonathan Andrew (2007). *Geochronology of weathering and landscape evolution, Hamersley Iron Province, Australia* PhD Thesis, School of Physical Sciences, University of Queensland.

Heim, J.A., Vasconcelos, P.M., Shuster, D.L., Farley, K.A., and Broadbent, G., 2006, Dating paleochannel iron ore by (U-Th)/He analysis of supergene goethite, Hamersley province, Australia: Geology, v. 34, no. 3, p. 173.

Kneeshaw, M., and Morris, R.C., 2014, The Cenozoic detrital iron deposits of the Hamersley Province, Western Australia: Australian Journal of Earth Sciences, v. 61, no. 4, p. 513–586.

Lascelles, D.F., 2012, Banded iron formation to high-grade iron ore: a critical review of supergene enrichment models: Australian Journal of Earth Sciences, v. 59, no. 8, p. 1105–1125.

Müller, R.D., Seton, M., and Zahirovic, S., 2016, Ocean basin evolution and global-scale plate reorganization events since Pangea breakup: Annual Review of Earth and Planetary Science, v. 44, p 107-138.

Ramanaidou, E.R., Morris, R.C., and Horwitz, R.C., 2003, Channel iron deposits of the Hamersley Province, Western Australia: Australian Journal of Earth Sciences, v. 50, no. 5, p. 669–690.

Sharp, Z. D., 1990, A laser-based microanalytical method for the *in-situ* determination of oxygen isotope ratios of silicates and oxides: Geochimica et Cosmochimica Acta, v. 54, p. 1353-1357.

Shuster, D. L., Vasconcelos, P. M., Heim, J. A., & Farley, K. A., 2005, Weathering geochronology by (U-Th)/He dating of goethite: Geochimica Et Cosmochimica Acta, v. 69, p. 659–673.

Schwertmann U. 1988. Occurrence and forma- tion of iron oxides in various pedoenvironments, *in* Iron in Soils and Clay Minerals, v217, pp. 267–308

Valley, J. W., Kitchen, N., Kohn, M. J., Niendorf, C. R., & Spicuzza, M. J., 1995. UWG-2, a garnet standard for oxygen isotope ratios: strategies for high precision and accuracy with laser heating: Geochimica et Cosmochimica Acta, v. 59, p. 5223-5231.

Vasconcelos, P. M., Heim, J. A., Farley, K. A., Monteiro, H., & Waltenberg, K., 2013, 40Ar/39Ar and (U–Th)/He – 4He/3He geochronology of landscape evolution and channel iron deposit genesis at Lynn Peak, Western Australia: Geochimica Et Cosmochimica Acta, v. 117, p. 283–312.

Wessel, P., and Müller, R.D., 2015, Plate Tectonics, *in Treatise on Geophysics, 2nd edition,* Schubert, Gerald ed., vol. 6, pp. 45-93.